Synthesis,structure and electrochemical performance of Eldfellite, $NaFe(SO_4)_2$, doped with SeO_4, HPO_4 and PO_3F

Trussov, Ivan; Kokhmetova, Saule ; Driscoll, Laura; Smith, Ronald; Berry, Frank; marco, jose; Galeyeva, AlinaK. ; Kurbatov, Andrey ; Slater, Peter

DOI:
10.1016/j.jssc.2020.121395

Document Version
Peer reviewed version

Citation for published version (Harvard):
Trussov, I, Kokhmetova, S, Driscoll, L, Smith, R, Berry, F, marco, J, Galeyeva, A, Kurbatov, A & Slater, P 2020, 'Synthesis,structure and electrochemical performance of Eldfellite, $NaFe(SO_4)_2$, doped with SeO_4, HPO_4 and PO_3F', *Journal of Solid State Chemistry*, vol. 289, 121395. https://doi.org/10.1016/j.jssc.2020.121395

Synthesis, structure and electrochemical performance of Eldfellite, $NaFe(SO_4)_2$, doped with SeO_4, HPO_4 and PO_3F⋆

Ivan A. Trussov[a,b,*], Saule T. Kokhmetova[c], Laura L. Driscoll[b], Ronald Smith[d], Frank J. Berry[b], José F. Marco[e], Alina K. Galeyeva[c], Andrey P. Kurbatov[c], Peter R. Slater[b]

[a] *Skoltech Center for Energy Science and Technology, Skolkovo Institute of Science and Technology, Moscow, 121205, Russian Federation*
[b] *School of Chemistry, University of Birmingham, Birmingham, B15 2TT, UK*
[c] *Center of Physical Chemical Methods of Research and Analysis, al-Farabi Kazakh National University, Almaty, 050012, Kazakhstan*
[d] *ISIS Facility, Rutherford Appleton Laboratory, Harwell Oxford, Didcot, OX11 0QX, UK*
[e] *Instituto de Quimica Fisica "Rocasolano", CSIC, Serrano 119, Madrid, 28006, Spain*

Abstract

$NaFe(SO_4)_2$ materials partially substituted with SeO_4^{2-}, HPO_4^{2-} and PO_3F^{2-} were prepared and investigated as possible cathode materials for sodium-ion batteries. Neutron diffraction and Raman spectroscopy studies confirmed the successful incorporation of SeO_4^{2-} and HPO_4^{2-}, while the Raman studies suggested that significant hydrolysis of PO_3F^{2-} had occurred during the synthesis. The effective diffusion coefficients were determined from conductivity and electrochemical kinetics studies, showing low Na ion diffusion. Galvanostatic and cyclic voltammetry investigations demonstrated more significant degradation and a narrowing of the electrochemical stability window for the doped materials, which was most significant for the SeO_4 and HPO_4 doped samples. Therefore, while doped $NaFe(SO_4)_2$ were successfully prepared, the best electrochemical performance was shown for the undoped system.

Keywords: Eldfellite, Na-ion, Sodium iron sulphate, Neutron diffraction

1. Introduction

The growing demand for low cost large-scale energy storage to balance the intermittency of renewable energy technologies is driving renewed interest in Na ion batteries, which are viewed as lower cost alternatives to lithium-ion batteries. As a result, there is renewed interest in the development of new cathode materials for Na ion batteries. While layered Na transition metal oxide materials are currently the favoured cathode materials[1, 2, 3, 4], there is growing interest in alternative materials containing oxoanion groups, as for Li ion batteries. In this respect, a wide range of such materials have been investigated: including $Na_3V_2(PO_4)_3$[5, 6, 7, 8], $NaFePO_4$[9, 10], $Na_2MnP_2O_7$[11], $Na_4Co_3(PO_4)_2P_2O_7$[12], $Na_3V_2O_2(PO_4)_2F$ [13, 14, 15, 16], $Na_{2.5}Fe_{1.75}(SO_4)_3$[17], Na_2FeSiO_4[18], $NaFe(SO_4)_2$[19].

As shown by the examples above, the focus of this research has been on systems containing a single oxoanion, despite the potential for tweaking both structure and properties by substitution on the oxoanion site. Recently we have illustrated the successful isovalent substitution of SO_4^{2-} by SeO_4^{2-} and PO_3F^{2-} in the bimetallic metal sulphates $Na_2M(SO_4)_2 \cdot 2H_2O$ (M = transition metal)[20], and structurally characterised the resultant phases obtained on dehydration[21]. In this work, we have extended such studies to investigate the effect of SeO_4^{2-}, PO_3F^{2-}, HPO_4^{2-} into the layered eldfellite structured $NaFe(SO_4)_2$. This phase was first reported by Balić-Žunic et al.[22] and more recently evaluated as a potential cathode for use in a Na-ion battery by Singh et al.[19]. In this latter work, $NaFe(SO_4)_2$ was shown to have a capacity near 80 mAh/g (at 0.1 C) for more than 80 cycles, with an average voltage of 3.2V versus sodium. Banerjee et al. predicted by DFT calculations that this material can be improved by transition metal substitution[23]. However, while partial substitution of iron with chromium demonstrated better thermal properties, the inactivity of the Cr^{2+}/Cr^{3+} redox couple meant that the electrochemical performance was poorer[24]. Given that the nature of oxoanion group plays a significant role in inductive effects in the lattice of these compounds[25], the partial substitution at this site is of interest. The partial substitution of the sulphate group with other 2- oxoanion changes the electrochemical performance of the $NaFe(SO_4)_2$ due to differences in sizes and inductive effects. Isovalent oxoanion dopants were chosen so that no other changes (e.g. Fe oxidation state, Na content) were affected in the doping strategy, and so any changes were purely down to the dopant itself. With this in mind, here we report a study of oxoanion doping in $NaFe(SO_4)_2$ to give $NaFe(SO_4)_{1.5}(X)_{0.5}$ (X=SeO_4, HPO_4 PO_3F), examining the effect on the structure and properties.

⋆Electronic Supplementary Information (ESI) available: See DOI: 10.5286/ISIS.E.RB1690407-1; 10.5286/ISIS.E.RB1690410-1; 10.5286/ISIS.E.RB1690411-1

*Corresponding author.
Email address: i.trussov@skoltech.ru (Ivan A. Trussov)

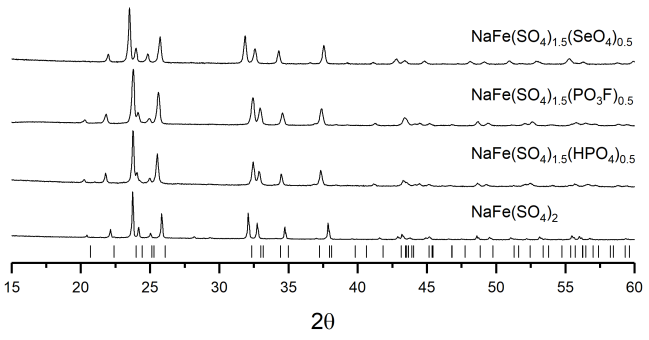

Figure 1: XRD patterns for $NaFe(SO_4)_{1.5}(X)_{0.5}$ (X = SeO_4, HPO_4, PO_3F, SO_4), tick marks designate Eldfellite, $NaFe(SO_4)_2$, structure

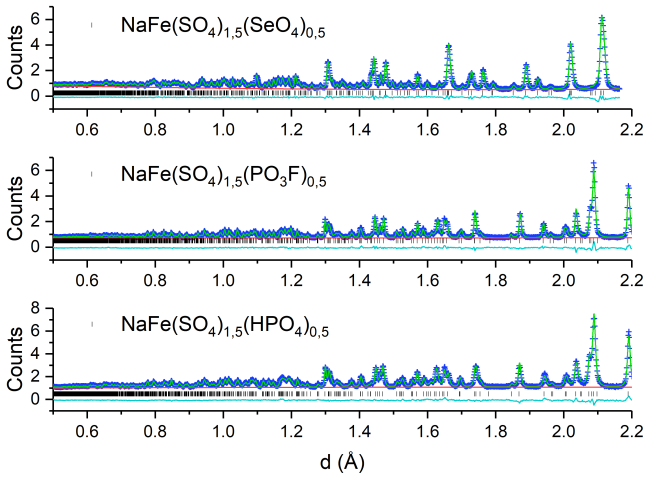

Figure 2: Observed, calculated and difference profiles from Rietveld refinement using ND data for $NaFe(SO_4)_{1.5}(X)_{0.5}$ (X = SeO_4, HPO_4, PO_3F)

2. Experimental

$NaFe(SO_4)_{1.5}(X)_{0.5}$ samples were prepared via a dissolution-evaporation route. In this facile route, stoichiometric amounts of $Fe_2(SO_4)_3$ and Na_2X (X=SeO_4, HPO_4, PO_3F, SO_4) were dissolved on heating in water. Evaporation of the water was then performed to obtain a thick slurry. This slurry was then dried for 12 hours at 150 °C in a drying oven; the powder was then ground and heated in an alumina crucible for 12 hours at 300 °C in a furnace. The obtained products were then analysed by powder XRD with data collected in Bragg-Brentano reflection geometry on a Panalytical Empyrean diffractometer with copper X-ray source ($\lambda CuK_{\alpha 1}$=1.54056Å, $\lambda CuK_{\alpha 2}$=1.54439Å) equipped with Pixcel 2D detector. Time of flight powder neutron diffraction (TOF) data were collected on the POLARIS diffractometer at the ISIS pulsed spallation source (Rutherford Appleton Laboratory, Harwell, UK)[26]. 3g of powder were loaded into 8 mm diameter thin-walled cylindrical vanadium sample cans. Data were collected at room temperature for 150 μAh proton beam energy to the ISIS target for each sample. Structure refinements (doped systems: neutron diffraction data, undoped system: X-ray diffraction data) were performed by the Rietveld method with the program GSASII[27].

In order to investigate the thermal stability and possible presence of water or carbonate in the samples, thermogravimetric analysis (TGA-MS, Netzsch) was performed at a rate of 10 °C/min to 400 °C in a nitrogen atmosphere with the MS detection of volatile substances for m/z = 18, 44 and 64 corresponding to water, carbon dioxide and sulphur dioxide. In order to determine more information on the oxoanion groups, Fourier transform infrared spectroscopy (Perkin Elmer FTIR Spectrum Two) as well as Raman spectroscopy (Renishaw inVia) data were collected. SEM images were collected on a Philips XL-30 FEG Environmental SEM with Oxford Inca EDS.

In order to determine more information on the Fe oxidation state, ^{57}Fe Mössbauer spectra were recorded in constant acceleration mode using a 25mCi ^{57}Co/Rh source. All spectra were computer fitted and all chemical isomer shift data are quoted relative to metallic iron at room temperature.

The conductivities of the obtained pellets were measured in air by electrochemical impedance spectroscopy (EIS) using a PSM impedance analyser within a frequency range 1 – 10^6 Hz. Measurements were carried on in the temperature range 50–300 °C on cooling in dry N_2 atmosphere. Pellets were coated on both sides with silver paste, which was dried at 150 °C for 2 hours. Zview software was used to analyse the obtained data[28]. The activation energy was calculated using the Arrhenius equation:

$$\sigma = Ae^{-\frac{E_a}{RT}}$$

where σ is the conductivity, A is the pre-exponential coefficient, E_a is the activation energy, R is the gas constant and T is the temperature. The diffusion coefficients were calculated using the Nernst-Einstein relation:

$$D = \frac{\sigma k_B T}{Z^2 \bar{e}^2 n}$$

where k_B is the Boltzmann constant, Z is the ion charge, $\bar{e}$ is the electron charge and n is charge carrier concentration (number of Na cations per unit-cell volume)[29, 30, 31].

Before the electrochemical measurements, the samples were ground in the Pulverisette 6 planetary ball mill in agate jar with hexane at 400 rpm for 9 hours. The particle sizes of the obtained powders were measured by laser diffraction (Horiba Partica Analyzer LA-960). For the electrochemical measurements in three electrode cell, the composite cathode slurry of weight ratio 70:20:10 active material, carbon black Timcal Super C45 (MTI KJ GROUP), PVdF, (SigmaAldrich) (3% solution in N-Methyl-2-pyrrolidone (NMP, SigmaAldrich, 99.9%)) was mixed in a ball mill and coated on to aluminium foil; this was then dried under a vacuum at 120 °C for 12 hours to obtain working electrodes. The three electrode cells were assembled with a Na metal electrode as reference, Pt-counter electrode and working electrode in 1M $NaClO_4$ in DMC/EC (1:1 ratio) electrolyte in the glove box under argon. The cell performances were evaluated using a potentiostat/galvanostat Autolab PGSTAT302N.

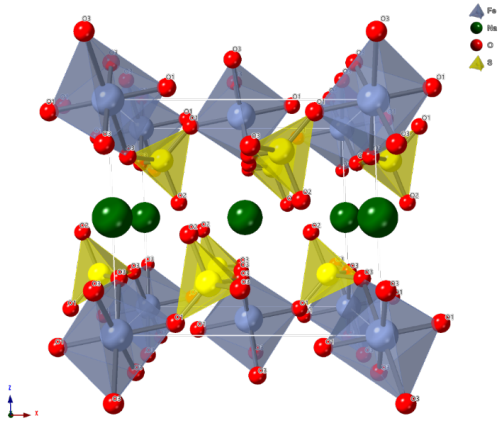

Figure 3: Structure of Eldfellite $NaFe(SO_4)_2$. Green sphere is a sodium, red is an oxygen, blue is an iron, and yellow is a sulphur.

3. Results and discussion

3.1. Diffraction study

The XRD data (Fig. 1) indicated the successful synthesis of $NaFe(SO_4)_{1.5}(X)_{0.5}$ (X is SeO_4, HPO_4, PO_3F, SO_4). The data indicated that all materials were isostructural without any traces of impurity phases.

Neutron diffraction (ND) data were collected for the doped materials and the structures were refined using the Rietveld method, with the previously reported structural model for $NaFe(SO_4)_2$ (space group $C12/m1$) used[22] (Fig. 2). For comparison, we also prepared undoped $NaFe(SO_4)_2$ and performed a structure refinement using the XRD data. The obtained cell parameters for both doped and undoped samples are shown in table 1.

As shown previously, the structure of $NaFe(SO_4)_2$ consists of corner sharing FeO_6 octahedra and SO_4 tetrahedra forming a triple layer SO_4–FeO_6–SO_4 perpendicular to the c axis with Na ions lying between these layers (Fig. 3). It has been proposed that the relatively rigid framework of layers allows a facile change in size of the cell along the c axis without decomposition during Na intercalation-deintercalation into these layers.

From the cell parameter data, it is clear that the unit cell expands on doping, with the largest expansion on selenate doping. In all cases, an expansion along the a and b axis is observed. However, for the samples doped with HPO_4^{2-}, PO_3F^{2-}, a contraction along the c axis is observed.

The refined occupancies confirm successful incorporation of the dopants (Tables 2-3). An attempt to refine the sodium occupancies showed no significant deviations from full occupancy, as expected. However, the refined anisotropic thermal displacement parameters demonstrated significantly prolate ellipsoidal shape for Na site suggesting split site disorder. The Na was therefore shifted off-site, and this was successfully refined with the overall sodium site occupancy fixed to 1 (1/4 for a single site).

Selected bond distances are given in table 4, and these show a particular increase in average distance for the selenate doped sample, as expected, while there is little change in the Fe-O distances.

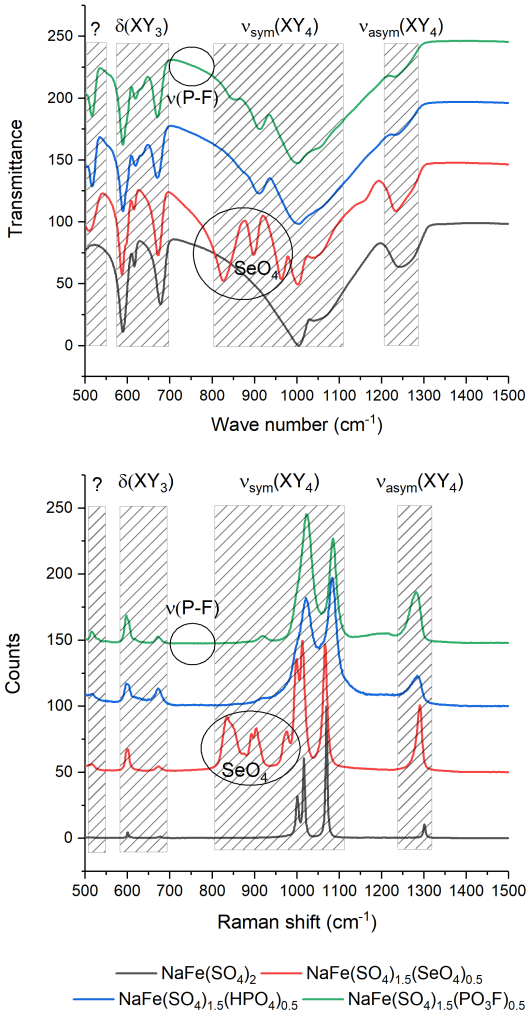

Figure 4: IR (top) and Raman (bottom) spectra of $NaFe(SO_4)_{1.5}(X)_{0.5}$ (X = SeO_4, HPO_4, PO_3F, SO_4)

For the PO_3F^{2-} doped sample, it was expected that there may be a significant change in one of the average S/P-O bond lengths, as a result of the P-F bond, assuming there is an ordered arrangement for the PO_3F^{2-} group. However, the data showed this not to be the case. Further discussion on this sample is outlined in the Raman data section. For the HPO_4^{2-} doped sample, the H position could not be defined, most likely due to random distribution and high thermal motion. However, considering the observed contraction along the c direction, we suspect that the proton is located pointing at adjacent layers to allow the formation of hydrogen bonds between layers and hence a contraction in this direction.

3.2. Vibrational spectra

In order to gather more information on these materials, IR and Raman spectra were recorded (Fig. 4). In all cases corresponding spectra are relatively similar showing the same general bands. The bands from the SO_4^{2-}, HPO_4^{2-}, SeO_4^{2-} and PO_3F^{2-} oxoanions in most cases can be distinguished separately as tetrahedral (T_d) anions, however overlapping of the

Table 1: Cell parameters and refinement quality indexes for $NaFe(SO_4)_{1.5}(X)_{0.5}$ (X = SeO_4, HPO_4, PO_3F, SO_4)

$C12/m1$	SeO_4^{2-}	PO_3F^{2-}	HPO_4^{2-}	SO_4^{2-}
a(Å)	8.0786(3)	8.1441(3)	8.1445(4)	8.0227(1)
b(Å)	5.2203(2)	5.1920(2)	5.1942(2)	5.1596(1)
c(Å)	7.1709(3)	7.0199(3)	7.0184(3)	7.1506(1)
$\gamma(^o)$	92.311(2)	91.684(2)	91.401(3)	92.097(1)
Volume($Å^3$)	302.169(29)	296.705(27)	296.822(31)	295.791(9)
R_{wp}	1.90%	2.16%	1.84%	2.09%
GOF	1.81	1.92	1.94	1.83

Table 2: Structural parameters obtained for $NaFe(SO_4)_{1.5}(X)_{0.5}$ (X = SeO_4, HPO_4, PO_3F)

Atom	Multiplicity	x	y	z	Fractional occupancy	U_{eq} x 100($Å^2$)
$NaFe(SO_4)_{1.5}(SeO_4)_{0.5}$						
Na	8	0.0226(14)	0.0402(10)	0.5094(25)	0.25	1.00(37)
Fe	2	0	0	0	1	0.70(5)
S	4	0.3624(3)	0	0.2260(3)	0.727(8)	0.63(5)
Se	4	0.3624(3)	0	0.2260(3)	0.273(8)	0.63(5)
O1	4	0.2375(2)	0	0.0598(2)	1	1.20(6)
O2	4	0.2906(2)	0	0.4070(2)	1	2.40(5)
O3	8	0.4716(1)	0.2370(2)	0.2016(2)	1	1.80(4)
$NaFe(SO_4)_{1.5}(PO_3F)_{0.5}$						
Na	8	0.0306(8)	0.0422(12)	0.5018(12)	0.25	1.75(25)
Fe	2	0	0	0	1	0.90(7)
S	4	0.3619(3)	0	0.2242(4)	0.727(22)	0.60(7)
P	4	0.3619(3)	0	0.2242(4)	0.273(22)	0.60(7)
O1	4	0.2343(2)	0	0.0688(3)	1	1.40(8)
O2	4	0.2896(2)	0	0.4143(3)	1	2.50(7)
O3	8	0.4648(2)	0.2354(2)	0.2044(2)	1	1.50(6)
$NaFe(SO_4)_{1.5}(HPO_4)_{0.5}$						
Na	8	0.0268(12)	0.0420(16)	0.5118(24)	0.25	1.00(49)
Fe	2	0	0	0	1	0.90(7)
S	4	0.3602(4)	0	0.2244(4)	0.732(21)	0.56(7)
P	4	0.3602(4)	0	0.2244(4)	0.268(21)	0.56(7)
O1	4	0.2348(2)	0	0.0686(3)	1	1.20(8)
O2	4	0.2894(2)	0	0.4154(3)	1	2.50(7)
O3	8	0.4640(2)	0.2356(3)	0.2051(2)	1	1.50(5)

Table 3: Anisotropic Displacement Parameters $Å^2$ x 100 for $NaFe(SO_4)_{1.5}(X)_{0.5}$ (X = SeO_4, HPO_4, PO_3F)

Atom	U_{11}	U_{22}	U_{33}	U_{12}	U_{13}	U_{23}
$NaFe(SO_4)_{1.5}(SeO_4)_{0.5}$						
Na	0.53(53)	0.76(32)	1.72(33)	-0.18(17)	0.29(39)	-0.25(27)
Fe	0.62(6)	0.43(6)	1.11(6)	0	0.08(4)	0
O1	0.65(5)	0.97(5)	1.88(6)	0	0.06(5)	0
O2	2.14(6)	2.87(5)	2.15(5)	0	0.05(4)	0
O3	1.86(6)	1.48(4)	2.05(4)	-0.69(3)	-0.72(3)	0.99(3)
$NaFe(SO_4)_{1.5}(PO_3F)_{0.5}$						
Na	2.67(28)	1.51(40)	1.00(12)	-0.21(17)	0.79(27)	0.52(21)
Fe	0.71(7)	0.27(7)	1.83(7)	0	-0.35(6)	0
O1	1.22(8)	1.49(7)	1.51(8)	0	-0.70(6)	0
O2	3.62(7)	2.09(7)	1.76(8)	0	0.79(5)	0
O3	1.74(5)	1.29(6)	1.37(6)	-0.56(4)	-0.50(4)	0.55(4)
$NaFe(SO_4)_{1.5}(HPO_4)_{0.5}$						
Na	1.06(55)	1.19(54)	0.84(42)	-0.05(24)	0.02(46)	0.05(30)
Fe	0.42(7)	0.56(7)	1.62(7)	0	-0.07(6)	0
O1	0.42(8)	1.47(7)	1.60(8)	0	-0.48(5)	0
O2	3.90(7)	1.94(7)	1.70(8)	0	1.17(6)	0
O3	1.41(5)	1.12(5)	1.92(5)	-0.79(4)	-0.56(4)	0.47(4)

Table 4: Selected interatomic distances (Å) and it's multiplicity from TOF neutron Rietveld refinement of $NaFe(SO_4)_{1.5}(X)_{0.5}$ (X = SeO_4, HPO_4, PO_3F)

		$NaFe(SO_4)_{1.5}(SeO_4)_{0.5}$			
S/Se-O1	1	1.530(2)	Fe-O1	2	1.949(1)
S/Se-O2	1	1.443(2)	Fe-O3	4	2.013(1)
S/Se-O3	2	1.533(2)			
		$NaFe(SO_4)_{1.5}(PO_3F)_{0.5}$			
S/P-O1	1	1.484(2)	Fe-O1	2	1.955(2)
S/P-O2	1	1.474(2)	Fe-O3	4	2.013(1)
S/P-O3	2	1.490(1)			
		$NaFe(SO_4)_{1.5}(HPO_4)_{0.5}$			
S/P-O1	1	1.478(2)	Fe-O1	2	1.960(2)
S/P-O2	1	1.472(2)	Fe-O3	4	2.016(1)
S/P-O3	2	1.495(1)			

peaks does complicate the assignments in some cases. The proposed assignments are shown in table 5. In all cases the ν_1 symmetrical vibrations (XY_4) of SO_4 are located in a similar region of frequencies in the Raman as well as in the IR spectra. For the phosphate containing compound a small shift towards lower frequencies can be observed. This shift is most likely attributed to the overlapping of the peaks of PO_4 and SO_4 groups which therefore couldn't be individually distinguished accurately. The shift in the SeO_4 group compared to the SO_4 group is clearer, with the former found in the expected region 830-850 cm^{-1} in both IR and Raman spectra. The ν_3 asymmetric vibrations (XY_4) for SO_4 were located in the same region for all compounds with a slight shift towards higher frequencies for the doped phases. The same vibration mode peaks of the SeO_4 group are observed in the expected range as well. The ν_3 vibrations are found at lower frequencies than expected for the PO_4 group. The $\nu_4(f_2)\delta(XY_3)$ vibrations of SO_4 group are very consistent for all compounds and located at the same energy (600 cm^{-1} and 673 cm^{-1}). However, there is splitting of these peaks for $NaFe(SO_4)_{1.5}(PO_3F)_{0.5}$ indicating local disorder on this site.

For the fluorophosphates doped sample, there was no trace of the expected ν(P−F) band in the region 700-800 cm^{-1}[32]. This may be an indication that the PO_3F^{2-} group has been hydrolysed during the synthesis leading to the formation of HPO_4^{2-} anion instead. In this regard, the overall similarity of the spectra for both HPO_4^{2-} and PO_3F^{2-} supports this suggestion. It would also explain the unexpected lower frequency location of the ν_3 asymmetric vibrations for $NaFe(SO_4)_{1.5}(PO_3F)_{0.5}$ as such a region was reported for hydrophosphate compounds by Frost et. al.[33]. The similar cell parameters for the HPO_4^{2-} and PO_3F^{2-} doped samples also support this, although there might still be the presence of small amount of residual fluorine in the latter (see electrochemical measurements section).

An interesting additional band at around 515 cm^{-1} was observed for the doped samples. This peak was not present in the undoped system, and we suggest that it might be related to the asymmetry of FeO_6 caused by different anions. The larger signal of this band on the IR spectra suggests that there is significant polarisation associated with this mode.

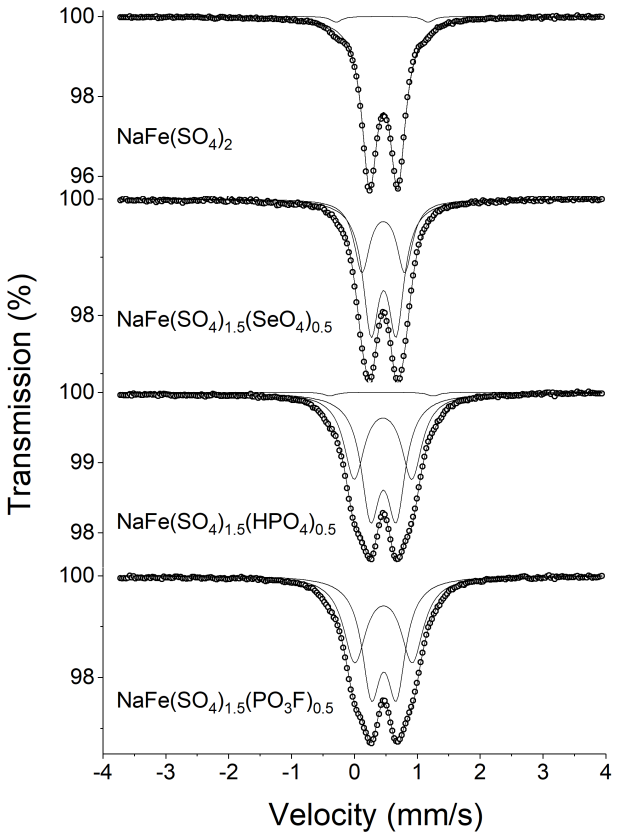

Figure 5: Mössbauer spectra recorded at 298K of $NaFe(SO_4)_{1.5}(X)_{0.5}$ (X = SeO_4, HPO_4, PO_3F, SO_4)

3.3. Mössbauer spectroscopy

The ^{57}Fe Mössbauer spectra recorded at 298K are shown in Fig. 5 and the ^{57}Fe Mössbauer parameters are shown in Table 6.

We associate the small (<2%) components in the spectra recorded from $NaFe(SO_4)_2$ and $NaFe(SO_4)_{1.5}(HPO_4)_{0.5}$ with the presence of a small impurity phase which is below the limits of detection by X-ray powder diffraction. The chemical isomer shifts of all spectral components were characteristic of Fe^{3+}. The values are at the higher end of the positive range expected for Fe^{3+} indicative of higher ionicity, which is normal for iron sulphate compounds[34]. The spectrum recorded from $NaFe(SO_4)_2$ showed a single quadrupole split absorption with Δ = 0.45 mm/s which we attribute to Fe^{3+} coordinated to only SO_4 units. Similar sites were observed in the spectra recorded from the SeO_4^{2-}, HPO_4^{2-} and PO_3F^{2-} doped materials. However, the spectra recorded from these doped materials also showed an additional doublet with larger quadrupole splitting indicative of the distorting effect of these dopants on the environment of the Fe^{3+} ions to which they are coordinated, by reason of their increased size and polarisabilty. The similar parameters recorded from the materials in which X = HPO_4 and PO_3F supports the evidence from Raman spectroscopy (see above) for hydrolysis of the fluorophosphate group to a hydrophosphate unit in $NaFe(SO_4)_{1.5}(PO_3F)_{0.5}$.

Table 5: Assignments of the IR and Raman Spectra of $NaFe(SO_4)_{1.5}(X)_{0.5}$

Assignment	Band position, cm^{-1} (intensity)			
	$NaFe(SO_4)_2$	$NaFe(SO_4)_{1.5}(SeO_4)_{0.5}$	$NaFe(SO_4)_{1.5}(HPO_4)_{0.5}$	$NaFe(SO_4)_{1.5}(PO_3F)_{0.5}$
$\nu_1(a_1)\nu_{sym}(XY_4)$	1000.8(30) (SO_4)	832.7(32) (SeO_4)	916.1(5) (PO_4)	922.6(3) (PO_4)
	1016.4(60) (SO_4)	849.2(27) (SeO_4)		914.8(3) (PO_4)
	1069.6(100) (SO_4)		999.7(18) (SO_4/PO_4)	
		973.2(24) (SO_4)	1022.1(66) (SO_4/PO_4)	1010.3(46) (SO_4/PO_4)
		998.4(71) (SO_4)	1059.5(18) (SO_4/PO_4)	1026.0(89) (SO_4/PO_4)
		1013.1(86) (SO_4)	1083.5(82) (SO_4/PO_4)	1084.5(75) (SO_4/PO_4)
		1066.2(94) (SO_4)		
$\nu_3(f_2)\nu_{asym}(XY_4)$	1300.9(10) (SO_4)	874.3(4) (SeO_4)	1132.1(5) (PO_4)	1180.7(6) (PO_4)
		891.8(16) (SeO_4)	1211.7(6) (PO_4)	1211.2(6) (PO_4)
		904.5(28) (SeO_4)		
			1270.5(11) (SO_4)	1284.3(28) (SO_4)
		1288.6(50) (SO_4)	1286.1(16) (SO_4)	1271.1(24) (SO_4)
$\nu_4(f_2)\delta(XY_3)$	600.2(5) (SO_4)	599.7(18) (SO_4)	599.4(15) (SO_4)	596.2(16) (SO_4)
				602.5(13) (SO_4)
	676.5(1) (SO_4)	672.9(3) (SO_4)	672.1(12) (SO_4)	672.5(5) (SO_4)
			627.6(3) (PO_4)	619.1(1) (PO_4)
Unknown		514.3(4)	516.3(5)	514.3(5)
				519.4(5)
				530.4(1)

Table 6: ^{57}Fe Mössbauer parameters recorded from materials of composition $NaFe(SO_4)_{1.5}(X)_{0.5}$ (X = SeO_4, HPO_4, PO_3F) at 298K

Compound	$\delta \pm 0.02$ (mm/s)	$\Delta \pm 0.04$ (mm/s)	Area $\pm 5\%$	Comment
$NaFe(SO_4)_2$	0.46	0.45	98	
	0.44	1.46	2	Impurity
$NaFe(SO_4)_{1.5}(SeO_4)_{0.5}$	0.46	0.40	64	
	0.46	0.68	36	
$NaFe(SO_4)_{1.5}(PO_3F)_{0.5}$	0.47	0.40	52	
	0.46	0.91	48	
$NaFe(SO_4)_{1.5}(HPO_4)_{0.5}$	0.46	0.41	55	
	0.45	0.92	44	
	0.43	1.64	1	Impurity

3.4. Scanning electron microscopy

The SEM images of obtained materials exhibited similar planar layered structures (Fig. 6). All structures consist of platelets of agglomerated layers.

3.5. Thermogravimetric analysis

As was expected, all the synthesised compounds demonstrated relatively low decomposition temperatures (Fig. 7). While undoped $NaFe(SO_4)_2$ was stable up to ~570 °C, the doped materials were less thermally stable, as illustrated by weight losses above 350 °C.

The peak m/z 64 corresponding to SO_2^+ appeared only above 600 °C in every case. Both hydrophosphate and fluorophosphate doped compounds decomposed with significant water elimination, which can be correlated with a condensation of two hydrogenphosphate anion into a pyrophosphate anion. The fact that the data for the fluorophosphate doped compound are similar for the hydrogenphosphate doped compound, further supports the hypothesis that hydrolysis of the fluorophosphategroup has occurred during the synthesis.

3.6. Ionic conductivity study

Conductivity measurements were performed on pellets sintered at 350 °C. Pellet densities showed relatively high values (~75%) for such low temperature sintering. However, due to the very low conductivity, impedance data could not be resolved into bulk and grain boundaries and so total conductivities are reported (fitted with a single semi-circle - constant phase element with resistor in parallel). To perform accurate evaluation of activation energy and minimise instrumental error due to very low conductivity of samples only data in the temperature region 150−300 °C was used and room temperature conductivity values reported are extrapolated estimates (Fig. 8, table 7).

Estimated room temperature conductivities for undoped and selenate doped samples were found to be very similar near 10^{-14} S/cm (Table 7). Therefore estimated diffusion coefficients showed similar values (note, as highlighted above, these were obtained from total (bulk plus grain boundary) conductivity values). Activation energies for both samples are around 0.74 eV, slightly higher than the values calculated by Yu et al. (0.6 eV)[35].

On the other hand, the estimated conductivities for the phosphate doped compounds were two orders of magnitude higher, along with a lower activation energy. Such significant difference might be related to the presence of protons in the crystal lattice and, therefore, the observed conductivity is most likely due to mixed Na^+/H^+ conduction. Nearly equal values for the hydrophosphate and fluorophosphate doped samples once again suggested that the fluorophosphate has hydrolysed during the synthesis.

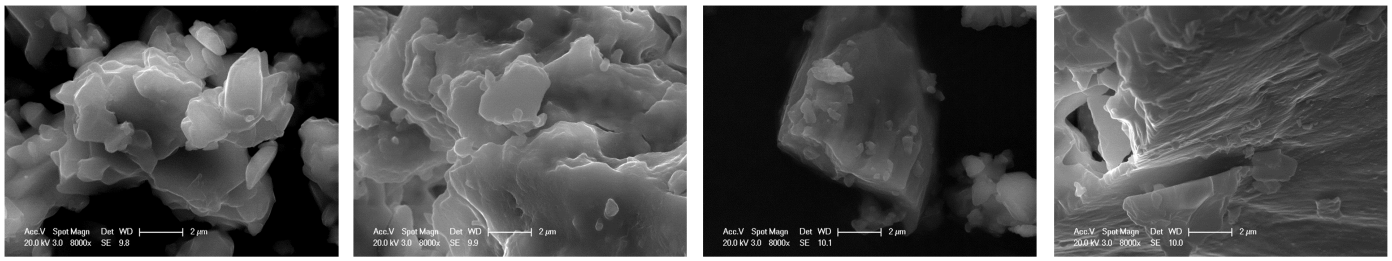

Figure 6: SEM images of $NaFe(SO_4)_{1.5}(X)_{0.5}$ (X=SeO_4, HPO_4, PO_3F, SO_4)

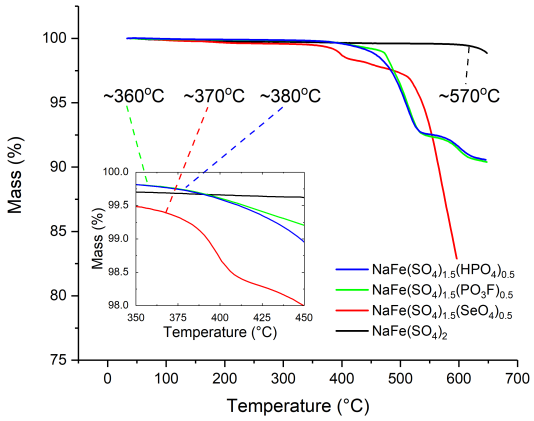

Figure 7: Thermogravimetric analysis data for $NaFe(SO_4)_{1.5}(X)_{0.5}$ (X = SeO_4, HPO_4, PO_3F, SO_4)

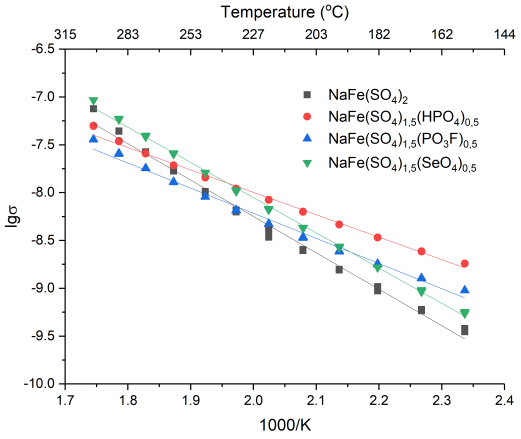

Figure 8: Conductivity Arrhenius plot for $NaFe(SO_4)_{1.5}(X)_{0.5}$ (X = SeO_4, HPO_4, PO_3F, SO_4)

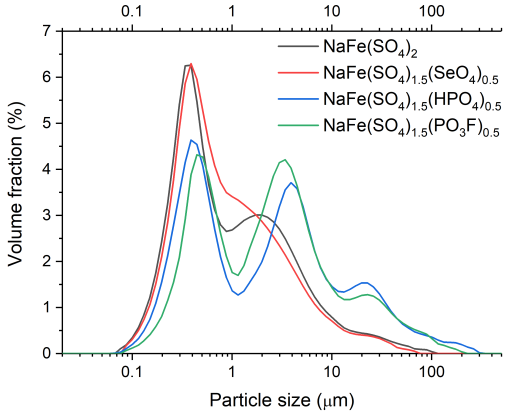

Figure 9: Powder particle size distribution according to laser diffraction analysis

Overall the ion diffusion is therefore low in these systems. Such poor ion-diffusion behaviour for oxyanion compounds is not unusual. For example, commercially successful cathode material $LiFePO_4$ has very similar conductivity[36]. The key for such successful utilisation of these systems in batteries is an electron conductive additive (carbon) and minimisation of the powder particle size to reduce ion diffusion path lengths.

3.7. Electrochemical study

Milled powders for the electrode testing were examined using the laser diffraction analysis. It was shown that the samples have several particle size populations. The average particle sizes of the powders were 1.36, 2.23, 4.47, 7.47 μm for $NaFe(SO_4)_{1.5}(X)_{0.5}$, where X = SO_4, SeO_4, HPO_4 and PO_3F respectively (Fig. 9).

Electrodes manufactured for electrochemical testing had 3 mg/cm^2 of active material loading with corresponding layer thickness of 20 μm. The cyclic voltammetry (CV) curves were recorded on all electrodes vs Na/Na^+ (Fig. 10).

Charge and discharge branches of the CV curves each had a peak in corresponding areas. The values of peak potentials matched for undoped and SeO_4 doped samples and had a small shift for HPO_4 and PO_3F doped equivalents. This could be attributed to different values of the equilibrium potentials of the doped materials with 3.26, 3.26, 3.25 and 3.22 V vs Na/Na^+ for X = SO_4, SeO_4, PO_3F and HPO_4 respectively. Considering

Table 7: Ion migration activation energy and diffusion coefficients at 293K for $NaFe(SO_4)_{1.5}(X)_{0.5}$ (X = SO_4, SeO_4, HPO_4, PO_3F)

Compound	Pellet density (% of theor.)	E_a (eV)	σ_{293K} (S/cm)	D_{293K} (cm^2/s) by EIS[a]	D_{293K} (cm^2/s) by CV[b]	Equilibrium potential (V)
$NaFe(SO_4)_2$	71%	0.75	2.37×10^{-14}	5.53×10^{-19}	1.4×10^{-13}	3.26
$NaFe(SO_4)_{1.5}(SeO_4)_{0.5}$	76%	0.73	5.56×10^{-14}	1.32×10^{-18}	3.8×10^{-14}	3.26
$NaFe(SO_4)_{1.5}(PO_3F)_{0.5}$	75%	0.52	1.18×10^{-12}	2.76×10^{-17}	3.1×10^{-13}	3.25
$NaFe(SO_4)_{1.5}(HPO_4)_{0.5}$	77%	0.46	4.92×10^{-12}	1.15×10^{-16}	1.4×10^{-14}	3.22

[a] Electrochemical Impedance Spectroscopy; [b] Cyclic Voltammetry.

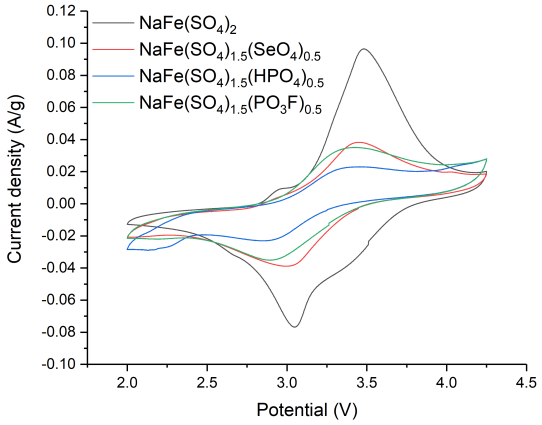

Figure 10: Cyclic voltammograms of the $NaFe(SO_4)_{1.5}(X)_{0.5}$ (X = SeO_4, HPO_4, PO_3F, SO_4). Scan rate 0.5 mV/s

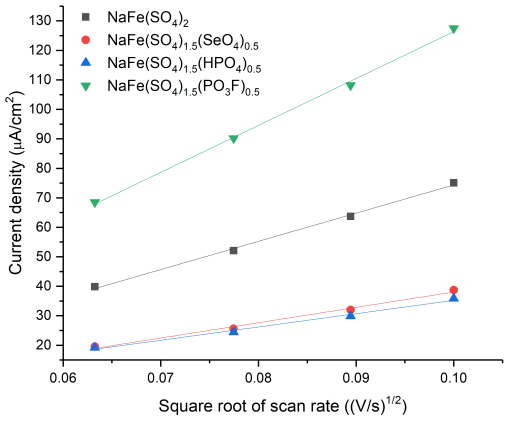

Figure 11: Dependence of the intercalation current on the square route of the CV sweep rate

reversible intercalation processes in these materials we can say that the exchange reaction at the electrode-electrolyte boundary is reversible as well. In this case the shift in the equilibrium potential of the doped materials in the working electrode towards the negative side might suggest an increase in sodium cation diffusion in the solid phase for these samples.

The charge and discharge peak areas of the CV curves (scan rate 0.5 mV/s) were nearly identical for each material confirming the high reversibility of the processes except for the SeO_4 doped sample. For this material the area of the cathodic peak exceeded the area of the anodic peak ~ 1.2 times suggesting the presence of additional process in the cathodic part responsible for the irreversible capacity and electrode degradation, most likely related to an additional contribution from selenate reduction.

The CV data were collected at different current sweep rates (4, 6, 8, 10 mV/s) in the range of 2.0-4.25V for all materials (except for $NaFe(SO_4)_{1.5}(SeO_4)_{0.5}$ (2.3-4.0V) due to the presence of parasitic reactions) to determine the intercalation/deintercalation diffusion coefficients via the Randles-Sevcik equation[37]:

$$i = 0.4463F\sqrt{(F/RT)}CA\sqrt{D}\sqrt{v}$$

where i is a current density on the active surface (CV peak); F is the Faraday number; R is the gas constant; T is a temperature; C is a molar concentration of the ions in the material (taken as a relation of material density to its molar mass, ~ 0.0096 mole/cm^3); A is an area of the active surface of the material; D is a diffusion coefficient; v is a current sweep rate. The area of the active surface of the material in electrode was calculated using the average particle size, active mass and density.

The collected data (Figure 1S, supplementary) showed that there is a specific shift of potentials with an increase of the sweep current rate to the cathodic and anodic sides for intercalation and deintercalation processes respectively. This agrees with Yu et al. who showed that this shift happens due to the ohmic polarization in the electrode similar to observed for $LiFePO_4$[37]. The current density on the surface of the active material was maximal for the PO_3F doped sample and minimal for the HPO_4 doped sample (Fig. 11). This correlates with the sodium diffusion coefficients obtained by CV confirming it to be completely limited by intercalation kinetics.

The largest diffusion coefficient was obtained for PO_3F and the smallest for HPO_4 doped samples. The large difference in diffusion values for hydrophosphate and fluorophosphate might indicate that the hydrolysis of the fluorophosphate may not be complete, leaving some residual fluorine, which aids the effective mobility of the sodium ion.

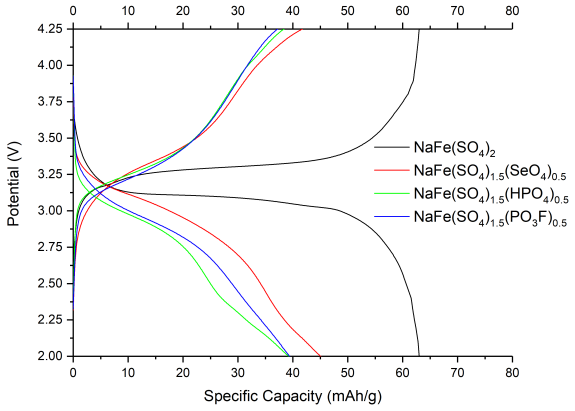

Figure 12: Charge-discharge curves of obtained materials at 0.1C vs Na/Na^+

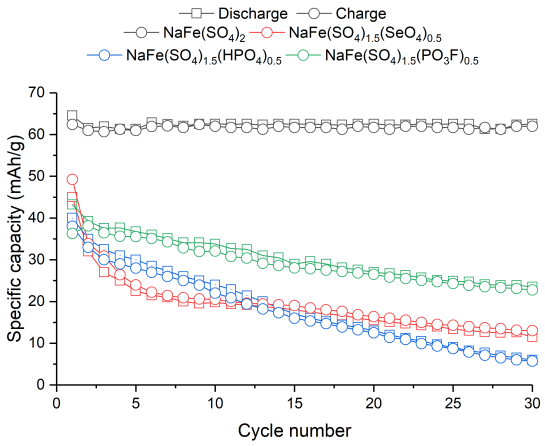

Figure 13: Specific capacities of obtained materials cycled at 0.1C rate

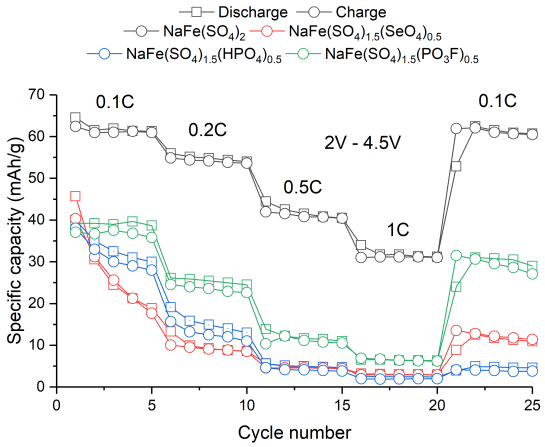

Figure 14: Specific capacities of obtained materials cycled at various C rates

The mismatch of diffusion coefficients obtained by CV and EIS experiments can be explained as follows. The pellet conductivity values represent total (bulk plus grain boundary) values, as it was not possible to resolve the bulk component. In addition, in the case of the EIS measurements, the Na ion is assumed to be a single charge carrier particle in the mass of the crystal. In case of CV measurements, the values relate to particles contacted with liquid electrolyte and the charge carrier is a combination of dissociated Na ion and electron transferred in the intercalation-deintercalation process, and is formally taken as the reducing particle in the CV model.

Galvanostatic charge/discharge tests (Fig. 12) at 0.1C for the first cycle showed capacities 63, 45, 39, 39 mAh/g for the SO_4, SeO_4, HPO_4, PO_3F doped materials respectively. The larger capacity, almost horizontal charge/discharge curve and high current CV peak suggested much lower polarizability and larger electrochemical reversibility for the undoped material. The same curves for the doped materials did not reveal a specific plateau demonstrating a gradual change in cycling limits. Furthermore, the galvanostatic curves for these materials demonstrated additional bending features indicating a change in the behaviour of the process. These additional features are much more noticeable on dQ/dV graphs for discharge (Figure 2S, Supplementary) process.

The most stable cycling behaviour was observed for undoped $NaFe(SO_4)_2$ (Fig. 13). After 30 cycles the material showed no degradation over the time. Doped materials do not demonstrate the same stability: the PO_3F doped sample lost nearly 30% of capacity over 30 cycles, while the HPO_4 doped sample showed almost no intercalation after 30 cycles. Such significant capacity loss for the hydrophosphate doped material might be related to the participation of the proton in the intercalation process, which results in the process being impeded. The PO_3F doped material instead degraded slower, probably, due to being more stable in presence of residual fluorine in the structure or as a minor impurity phase. The selenate doped material gave a significant loss of nearly 50% of initial capacity in the first five cycles and then gradually decreased to 13 mAh/g by the 30th cycle. The Coulomb efficiency of doped materials was between 80-95%. Considering the above mentioned excessive capacity of the cathodic process over the anodic we can assume that reduction of the selenate ion into selenite is occurring, with subsequent irreversible degradation of the structure.

Increasing the cycling current led to a significant decrease in the capacity of the materials (Fig. 14). At 1C the capacity decreased to almost half the original value (33 mAh/g) for the undoped material and more significantly for the doped samples (less than 10mAh/g), while the Coulombic efficiency is close to 100% for the undoped materials and between 80-100% for the doped samples. The undoped material showed the capacity at 0.1C close to the initial values after 20 cycles at different currents (0.1C-1C). The PO_3F doped material demonstrated a small capacity lowering, while the SeO_4 and HPO_4 doped samples revealed strong degradation under the same conditions.

To investigate whether structure degradation was the reason for the larger capacity loss of the SeO_4 and HPO_4 doped materials, we collected ex-situ XRD data of the working electrodes before and after cycling (Figure 3S, Supplementary). The XRD

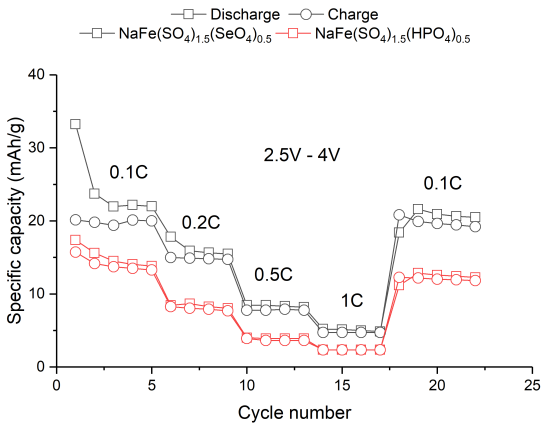

Figure 15: Specific capacities of obtained materials cycled at 0.1C rate in narrowed range (2.5V-4V)

patterns of the electrodes after cycling showed a significant decrease of Eldfellite peaks for the HPO_4 doped and complete absence for the SeO_4 doped sample, suggesting amorphisation of the cathode materials. The presence of additional bend features in the discharge curves (Fig. 12) suggested parasitic processes to degrade the material near the limits of the cycling range. The cycling of the fresh electrodes in a narrower range (2.5-4V) demonstrated much better behaviour with good capacity retention after 20 cycles at different currents (Fig. 15). This confirmed that, below 2.5V for cathodic and above 4V for anodic processes, the parasitic reactions related to dopants occur. This degrades the structure and resultant intercalation ability.

4. Conclusions

$NaFe(SO_4)_2$ partially substituted with ${SeO_4}^{2-}$, ${HPO_4}^{2-}$ and ${PO_3F}^{2-}$ were prepared and shown to be isostructural to $NaFe(SO_4)_2$ (Eldfellite). The studies confirmed the successful incorporation of ${SeO_4}^{2-}$ and ${HPO_4}^{2-}$, while the Raman/IR studies suggested that hydrolysis of ${HPO_4}^{2-}$ had occurred in the synthesis making this sample more similar to HPO_4 doped analogue with related proton conductivity. These represent the first examples of successful oxoanion doping in $NaFe(SO_4)_2$. While successful doping was demonstrated, galvanostatic testing of half-cells demonstrated deterioration of the cycling behaviour of the doped materials with narrowing of the electrochemical stability window, which was most significant for the SeO_4, and HPO_4 doped samples.

Overall, while the doped materials showed poor cycling behaviour in comparison to the undoped system, the prepared samples demonstrate the structural flexibility of the eldfellite framework, illustrating the ability to modify the oxoanion sites, while preserving the structure. Nevertheless, while in this system, the electrochemical performance was reduced on doping, it is possible that for other sulfate systems, such doping strategies may offer future promise.

Acknowledgements

We thank Bolashak International Scholarship (PhD scholarship for Ivan Trussov) and Ministry of Education and Science of the Republic of Kazakhstan (project AP05131849) for financial support. We also thank the STFC ISIS Facility for the provision of the neutron diffraction time.

References

[1] D. Zhou, W. Huang, X. Kang, F. Zhao, L. Zhao, Z. Deng, X. Yan, Y. Yu, M. Xiang, Titanium-doped P2-type Na0.67Co0.67Mn0.33-xTixO2(0 ≤ x ≤ 0.2) as Novel Cathodes for sodium ion batteries with superior-rate, International Journal of Electrochemical Science 13 (2) (2018) 2010–2021. doi:10.20964/2018.02.62.

[2] S. Kumakura, Y. Tahara, K. Kubota, K. Chihara, S. Komaba, Sodium and Manganese Stoichiometry of P2-Type Na2/3MnO2, Angewandte Chemie - International Edition 55 (41) (2016) 12760–12763. doi:10.1002/anie.201606415.

[3] L. Wang, J. Wang, X. Zhang, Y. Ren, P. Zuo, G. Yin, J. Wang, Unravelling the origin of irreversible capacity loss in NaNiO2for high voltage sodium ion batteries, Nano Energy 34 (February) (2017) 215–223. doi:10.1016/j.nanoen.2017.02.046.

[4] X. Sun, Y. Jin, C. Y. Zhang, J. W. Wen, Y. Shao, Y. Zang, C. H. Chen, Na[Ni0.4Fe0.2Mn0.4-xTix]O2: A cathode of high capacity and superior cyclability for Na-ion batteries, Journal of Materials Chemistry A 2 (41) (2014) 17268–17271. doi:10.1039/c4ta03828b.

[5] Y. Fang, L. Xiao, X. Ai, Y. Cao, H. Yang, Hierarchical Carbon Framework Wrapped Na3V2(PO4)3 as a Superior High-Rate and Extended Lifespan Cathode for Sodium-Ion Batteries, Advanced Materials 27 (39) (2015) 5895–5900. doi:10.1002/adma.201502018.

[6] Z. Jian, W. Han, X. Lu, H. Yang, Y.-S. Hu, J. Zhou, Z. Zhou, J. Li, W. Chen, D. Chen, L. Chen, Superior Electrochemical Performance and Storage Mechanism of Na3V2(PO4)3 Cathode for Room-Temperature Sodium-Ion Batteries, Advanced Energy Materials 3 (2) (2013) 156–160. doi:10.1002/aenm.201200558.

[7] S. Y. Lim, H. Kim, R. A. Shakoor, Y. Jung, J. W. Choi, Electrochemical and Thermal Properties of NASICON Structured Na3V2(PO4)3 as a Sodium Rechargeable Battery Cathode: A Combined Experimental and Theoretical Study, JOURNAL OF THE ELECTROCHEMICAL SOCIETY 159 (9) (2012) A1393–A1397. doi:10.1149/2.015209jes.

[8] Z. Jian, L. Zhao, H. Pan, Y.-S. Hu, H. Li, W. Chen, L. Chen, Carbon coated Na3V2(PO4)3 as novel electrode material for sodium ion batteries, ELECTROCHEMISTRY COMMUNICATIONS 14 (1) (2012) 86–89. doi:10.1016/j.elecom.2011.11.009.

[9] Y. Fang, Q. Liu, L. Xiao, X. Ai, H. Yang, Y. Cao, High-Performance Olivine NaFePO4 Microsphere Cathode Synthesized by Aqueous Electrochemical Displacement Method for Sodium Ion Batteries, ACS Applied Materials and Interfaces 7 (32) (2015) 17977–17984. doi:10.1021/acsami.5b04691.

[10] J. Kim, D.-H. H. Seo, H. Kim, I. Park, J.-K. K. Yoo, S.-K. K. Jung, Y.-U. U. Park, W. A. Goddard, K. Kang, W. A. Goddard III, K. Kang, Unexpected discovery of low-cost maricite NaFePO 4 as a high-performance electrode for Na-ion batteries, Energy Environ. Sci. 8 (2) (2015) 540–545. doi:10.1039/C4EE03215B.

[11] C. S. Park, H. Kim, R. A. Shakoor, E. Yang, S. Y. Lim, R. Kahraman, Y. Jung, J. W. Choi, Anomalous manganese activation of a pyrophosphate cathode in sodium ion batteries: a combined experimental and theoretical study., Journal of the American Chemical Society 135 (7) (2013) 2787–92. doi:10.1021/ja312044k.

[12] M. Nose, H. Nakayama, K. Nobuhara, H. Yamaguchi, S. Nakanishi, H. Iba, Na4Co3(PO4)2P2O7: A novel storage material for sodium-ion batteries, Journal of Power Sources 234 (2013) 175–179. doi:10.1016/j.jpowsour.2013.01.162.

[13] H. Jin, J. Dong, E. Uchaker, Q. Zhang, X. Zhou, S. Hou, J. Li, G. Cao, Three dimensional architecture of carbon wrapped multilayer Na3V2O2(PO4)2F nanocubes embedded in graphene for improved sodium ion batteries, J. Mater. Chem. A 3 (34) (2015) 17563–17568. doi:10.1039/C5TA03164H.

[14] R. K. B. Gover, P. Burns, A. Bryan, M. Y. Saidi, J. L. Swoyer, J. Barker, LiVPO4F: A new active material for safe lithium-ion batteries, Solid State Ionics 177 (26-32 SPEC. ISS.) (2006) 2635–2638. doi:10.1016/j.ssi.2006.04.049.

[15] T. Broux, T. Bamine, F. Fauth, L. Simonelli, W. Olszewski, C. Marini, M. Ménétrier, D. Carlier, C. Masquelier, L. Croguennec, Strong Impact of the Oxygen Content in Na3V2(PO4)2F3– yOy ($0 \leq y \leq 0.5$) on Its Structural and Electrochemical Properties, Chemistry of Materials 28 (21) (2016) 7683–7692. doi:10.1021/acs.chemmater.6b02659.

[16] Y. Kawabe, N. Yabuuchi, M. Kajiyama, N. Fukuhara, T. Inamasu, R. Okuyama, I. Nakai, S. Komaba, A Comparison of Crystal Structures and Electrode Performance between Na2FePO4F and Na2Fe0.5Mn0.5PO4F Synthesized by Solid-State Method for Rechargeable Na-Ion Batteries, Electrochemistry 80 (2) (2012) 80–84. doi:10.5796/electrochemistry.80.80.

[17] P. Barpanda, G. Oyama, S.-i. Nishimura, S.-C. Chung, A. Yamada, A 3.8-V earth-abundant sodium battery electrode, Nature Communications 5 (2014) 1–8. doi:10.1038/ncomms5358.

[18] S. Li, J. Guo, Z. Ye, X. Zhao, S. Wu, J. X. Mi, C. Z. Wang, Z. Gong, M. J. McDonald, Z. Zhu, K. M. Ho, Y. Yang, Zero-Strain Na2FeSiO4 as Novel Cathode Material for Sodium-Ion Batteries, ACS Applied Materials and Interfaces 8 (27) (2016) 17233–17238. doi:10.1021/acsami.6b03969.

[19] P. Singh, K. Shiva, H. Celio, J. B. Goodenough, Eldfellite, NaFe(SO4)2: an intercalation cathode host for low-cost Na-ion batteries, Energy Environ. Sci. 8 (10) (2015) 3000–3005. doi:10.1039/C5EE02274F.

[20] L. Driscoll, E. Kendrick, A. Wright, P. Slater, Investigation into the effect on structure of oxoanion doping in Na2M(SO4)2·2H2O, Journal of Solid State Chemistry 242 (2016) 103–111. doi:10.1016/j.jssc.2016.07.004.

[21] L. Driscoll, E. Kendrick, K. Knight, A. Wright, P. Slater, Investigation into the dehydration of selenate doped Na<inf>2</inf>M(SO<inf>4</inf>)<inf>2</inf>·2H<inf>2</inf>O (M = Mn, Fe, Co and Ni): Stabilisation of the high Na content alluaudite phases Na<inf>3</inf>M<inf>1.5</inf>(SO<inf>4</inf>)<inf>3-1.5x</inf>, Journal of Solid State Chemistry 258. doi:10.1016/j.jssc.2017.09.025.

[22] T. Balić-Žunić, A. Garavelli, P. Acquafredda, E. Leonardsen, S. P. Jakobsson, Eldfellite, NaFe(SO4)2, a new fumarolic mineral from Eldfell volcano, Iceland, Mineralogical Magazine 73 (2009) 51–57. doi:10.1180/minmag.2009.073.1.51.

[23] A. Banerjee, R. B. Araujo, R. Ahuja, Unveiling the thermodynamic and kinetic properties of NaxFe(SO4)2(x=0–2): toward a high-capacity and low-cost cathode material, J. Mater. Chem. A 4 (46) (2016) 17960–17969. doi:10.1039/C6TA05330K.

[24] U. Nisar, M. H. Gulied, R. A. Shakoor, R. Essehli, Z. Ahmad, A. Alashraf, R. Kahraman, S. Al-Qaradawi, A. Soliman, Synthesis and performance evaluation of nanostructured NaFe x Cr 1−X (SO 4) 2 cathode materials in sodium ion batteries (SIBs), RSC Advances 8 (57) (2018) 32985–32991. doi:10.1039/C8RA06583G.

[25] K. Nanjundaswamya, A. Padhi, J. Goodenough, S. Okada, H. Ohtsukab, H. Arai, J. Yamakib, Synthesis, redox potential evaluation and electrochemical characteristics of NASICON-related-3D framework compounds, Solid State Ionics 92 (1996) 1–10. doi:10.1016/S0167-2738(96)00472-9.

[26] R. I. Smith, S. Hull, M. G. Tucker, H. Y. Playford, D. J. McPhail, S. P. Waller, S. T. Norberg, The upgraded Polaris powder diffractometer at the ISIS neutron source, Review of Scientific Instruments 90 (11) (2019) 115101. doi:10.1063/1.5099568.

[27] B. H. Toby, R. B. Von Dreele, GSAS-II: The genesis of a modern open-source all purpose crystallography software package, Journal of Applied Crystallography 46 (2) (2013) 544–549. doi:10.1107/S0021889813003531.

[28] D. Johnson, ZView: A Software Program for IES Analysis, Version 3.1c, Scribner Associates Inc. (2009) 1990–2005.

[29] H. Sato, Some theoretical aspects of solid electrolytes, in: S. Geller (Ed.), Solid Electrolytes, Springer Berlin Heidelberg, Berlin, Heidelberg, 1977, pp. 3–39. doi:10.1007/3540083383_2.

[30] W. G. Zeier, S. Zhou, B. Lopez-Bermudez, K. Page, B. C. Melot, Dependence of the li-ion conductivity and activation energies on the crystal structure and ionic radii in Li6MLa2Ta 2O12, ACS Applied Materials and Interfaces 6 (14) (2014) 10900–10907. doi:10.1021/am4060194.

[31] A. Criado, P. Lavela, C. Pérez-Vicente, G. Ortiz, J. Tirado, Effect of chromium doping on Na3V2(PO4)2F3@C as promising positive electrode for sodium-ion batteries, Journal of Electroanalytical Chemistry 856 (2020) 113694. doi:10.1016/j.jelechem.2019.113694.

[32] M. Weil, M. Puchberger, E. Füglein, E. J. Baran, J. Vannahme, H. J. Jakobsen, J. Skibsted, Single-Crystal Growth and Characterization of Disilver(I) Monofluorophosphate(V), Ag2PO3F: Crystal Structure, Thermal Behavior, Vibrational Spectroscopy, and Solid-State 19F, 31P, and 109Ag MAS NMR Spectroscopy, Inorganic Chemistry 46 (3) (2007) 801–808. doi:10.1021/ic061765w.

[33] R. L. Frost, S. J. Palmer, Y. Xi, A Raman spectroscopic study of the mono-hydrogen phosphate mineral dorfmanite Na2(PO3OH)·2H2O and in comparison with brushite, Spectrochimica Acta Part A: Molecular and Biomolecular Spectroscopy 82 (1) (2011) 132–136. doi:10.1016/J.SAA.2011.07.015.

[34] G. J. Long, G. Longworth, P. Battle, A. K. Cheetham, R. V. Thundathil, D. Beveridge, A study of anhydrous iron(III) sulfate by magnetic susceptibility, Moessbauer, and neutron diffraction techniques, Inorganic Chemistry 18 (3) (1979) 624–632. doi:10.1021/ic50193a021.

[35] C.-J. Yu, S.-H. Choe, G.-C. Ri, S.-C. Kim, H.-S. Ryo, Y.-J. Kim, Ionic Diffusion and Electronic Transport in Eldfellite NaxFe(SO4)2, Physical Review Applied 8 (2) (2017) 024029. doi:10.1103/PhysRevApplied.8.024029.

[36] A. K. Padhi, K. S. Nanjundaswamy, J. B. D. Goodenough, Phospho-olivines as Positive-Electrode Materials for Rechargeable Lithium Batteries, Journal of The Electrochemical Society 144 (4) (1997) 1188. doi:10.1149/1.1837571.

[37] D. Y. W. Yu, C. Fietzek, W. Weydanz, K. Donoue, T. Inoue, H. Kurokawa, S. Fujitani, Study of LiFePO4 by Cyclic Voltammetry, Journal of The Electrochemical Society 154 (4) (2007) A253. doi:10.1149/1.2434687.